
High-Beam-Quality Meta-Grating Couplers for Large Collimated Free-Space Beams on Silicon-on-Insulator

Max Schittenhelm^{1,2} Sebastian Häfner^{1,2} Steffen Sauer^{1,2,3} Stefanie Kroker^{1,2,3,*}

¹Institut für Halbleitertechnik, Technische Universität Braunschweig, Hans-Sommer-Str. 66, 38106 Braunschweig, Germany

²Laboratory for Emerging Nanometrology, Langer Kamp 6a-b, 38106 Braunschweig, Germany

³Physikalisch-Technische Bundesanstalt, Bundesallee 100, 38116 Braunschweig, Germany

Email Address: *s.kroker@tu-braunschweig.de

Keywords: *Grating coupler, Silicon photonics, Beam shaping, Chip-to-free-space*

Photonic integrated circuits on the silicon-on-insulator (SOI) platform typically interface with free space via grating couplers, but scaling these to collimated beams with diameters beyond 100 μm requires a fundamentally different regime of extremely weak, spatially distributed coupling. While such large-area couplers have been demonstrated, their beam quality has remained largely uncharacterized, even though applications such as coupling into high-finesse resonators or trapping of cold atoms require both a large aperture and a near-Gaussian profile. This article presents an SOI meta-grating coupler that emits collimated, near-Gaussian beams of approximately 300 μm waist diameter. The design synthesizes the required emission profile from a spatially tailored coupling strength, realized by locally varying a sub-wavelength unit cell while independently setting the local emission angle. This approach achieves the very low coupling strengths required for large beams and yields a measured beam quality of $M^2 \leq 1.10$. The scheme extends directly to other target profiles, such as flat-top or higher-order modes, rendering meta-grating couplers a practical chip-to-free-space interface for mode-matching-sensitive applications.

1 Introduction

Photonic integrated circuits (PIC) based on the silicon-on-insulator (SOI) platform have become a cornerstone of modern integrated photonics. They combine compactness and mechanical robustness with access to the highly mature, CMOS-compatible fabrication technology [1, 2, 3]. This combination has made SOI the platform of choice for a wide range of applications from optical communications [4] to sensing [5, 6], LIDAR [7, 8] and quantum photonics [9].

A key enabling element for PICs is the interface between the on-chip and off-chip optical modes. Grating couplers (GCs) that connect the on-chip waveguides to off-chip optical fibers are now a well-established solution for this task and have been studied thoroughly [10, 11, 12, 13, 14, 15]. These grating couplers emit beams with diameters on the order of 10 μm to match the fiber's mode field diameter. Extending these couplers toward much larger beam radii and therefore toward collimated free-space beams, however, requires a fundamentally different coupling regime. The grating couplers must exhibit extremely small coupling strengths in order to extend the emission over several hundreds of microns.

Large beam size grating couplers have already found use in several applications such as 3D magneto-optical traps [16, 17, 18], sub-Doppler atomic spectroscopy [19] or on-chip laser stabilization [20]. In all these cases, the beam merely has to illuminate an atomic ensemble or vapor cell over a large area, so that the detailed beam quality is of secondary importance and was neither systematically optimized nor analyzed. A second class of applications places considerably stricter demands on the emitted beam. Efficient coupling into optical resonators, in particular, relies on a high beam quality to achieve good mode matching [21]. Beyond that, applications involving trapped atoms, for instance the coherent addressing of individual sites in optical lattices, can equally benefit from large, well-defined beams with low divergence [22, 23, 24].

The beam quality relevant to these applications is commonly quantified by the beam quality parameter M^2 , which describes how closely a beam approaches the diffraction-limited Gaussian case. A value of $M^2 = 1$ corresponds to an ideal Gaussian beam and thus sets the upper bound on the achievable overlap with a target mode such as that of an atomic trap or an optical resonator. While a low M^2 does not by itself guarantee good mode matching, which also depends on waist size, position, and wavefront curvature, it is a necessary precondition: no beam can exceed the overlap permitted by its M^2 . It is therefore a practically meaningful figure of merit for evaluating large-area, chip-emitted beams.

arXiv:2607.01477v1 [physics.optics] 1 Jul 2026

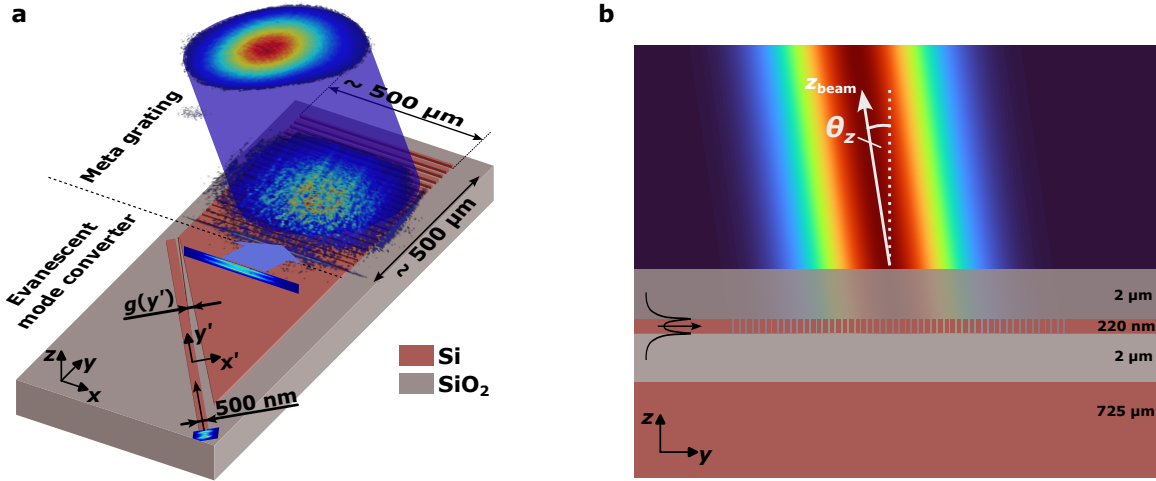


Figure 1: a) Schematic overview of the design consisting of an evanescent mode converter and a meta-grating coupler and b) the cross section of the grating coupler with the desired Gaussian beam emission. The portion of the beam that is emitted into the $-z$ -direction is omitted for the sake of visual clarity.

Several groups have reported grating couplers achieving large beam diameters exceeding $100\ \mu\text{m}$ [25, 26, 27, 28, 17, 29, 30, 31]. To the best of our knowledge, however, none of these has combined such a large output diameter with a beam quality sufficient to meet the demands of the most mode-matching-sensitive applications.

In this work, we present and experimentally validate an SOI meta-grating coupler design scheme that achieves large, collimated beams with excellent beam quality factors of $M^2 \leq 1.10$. Two designs with emission angles of -2° and -9° are implemented, which require only a single etch step with minimum feature sizes of $229\ \text{nm}$ and $110\ \text{nm}$, respectively. This performance is enabled by extending the sub-wavelength grating coupler approach of [23] through a locally tailored coupling-strength profile, supported by an evanescent mode converter as demonstrated in [17].

2 Design

The presented designs consist of two parts: the evanescent mode converter which expands the tightly confined mode from the waveguide (width of $500\ \text{nm}$) to the slab (width of $500\ \mu\text{m}$) and the meta-grating with variable coupling strength, as shown in Figure 1a. Together these two stages expand the mode field diameter to $300\ \mu\text{m}$ in the lateral and longitudinal direction, yielding a circular Gaussian beam. The TM_{00} mode was chosen as the operating mode since it is less confined along the z -direction compared to the TE_{00} mode, which allows for weaker interaction with the grating ridges and thus yields weaker coupling strengths. All designs discussed in this contribution use an SOI platform with a device layer thickness of $220\ \text{nm}$, as shown in Figure 1b, with an operating vacuum wavelength of $\lambda_0 = 1.55\ \mu\text{m}$.

2.1 Meta-grating coupler

Our design scheme builds upon the sub-wavelength grating concept introduced by Barona-Ruiz et al. [31], in which the coupling strength κ of a grating coupler is strongly reduced by exploiting symmetry breaking in a sub-wavelength waveguide. For symmetric ridge widths ($a = b$) and a sub-wavelength period $\Lambda_{\text{SWG}} < \lambda_{\text{mode}}$, the structure acts as an effective-medium waveguide and does not radiate. Introducing a small asymmetry ($a \neq b$) establishes a super-period $\Lambda = 2\Lambda_{\text{SWG}} > \lambda_{\text{mode}}$ that lies in the radiating regime, enabling emission profiles extending over several hundred micrometers [31]. In a homogeneous grating, however, the unit cell, and therefore κ , remains constant along the propagation direction, so the emitted near field decays exponentially (Figure 2a). This fixes the emission profile and precludes the high beam quality required by mode-matching-sensitive applications. Here we lift this constraint: by

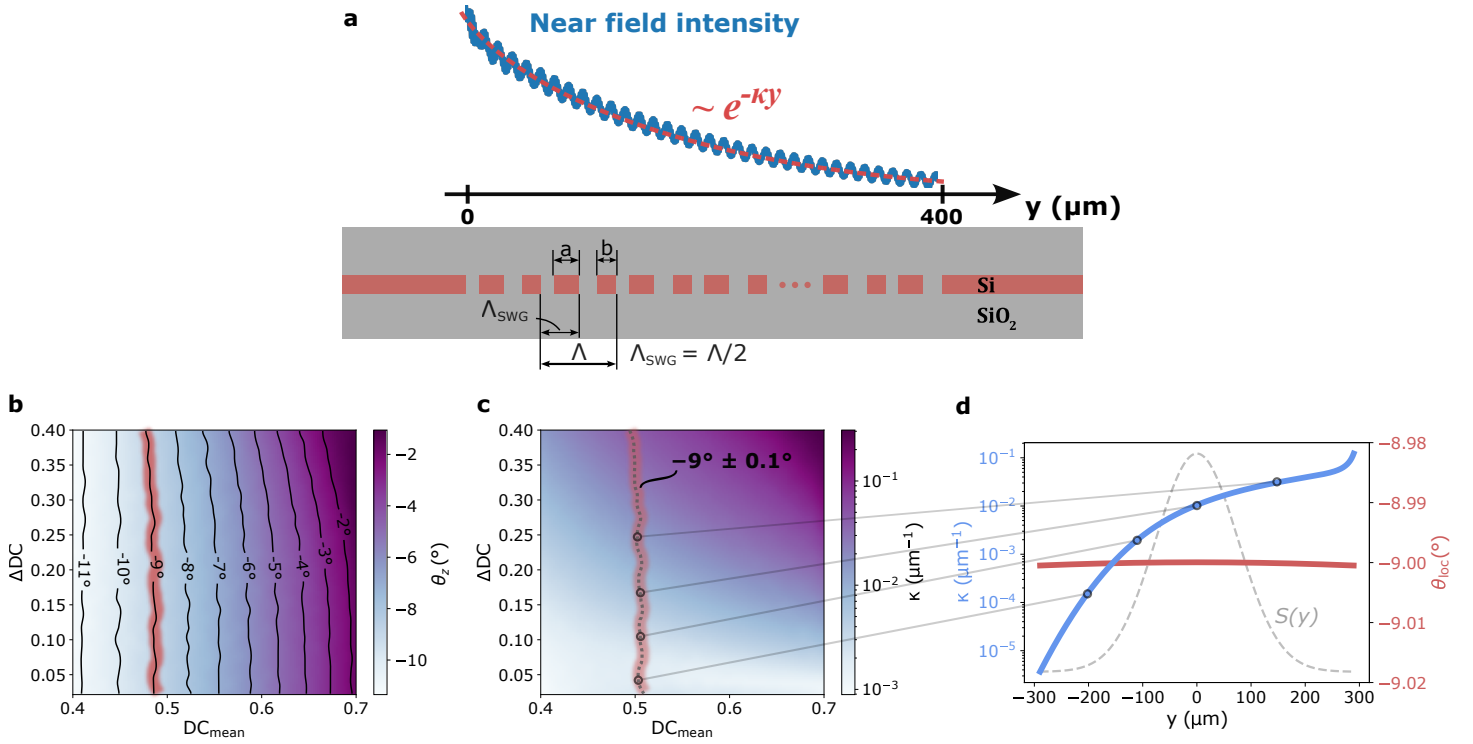


Figure 2: a) Cross section of a homogeneous sub-wavelength grating with ridge widths a and b , which emits an exponentially decaying near field intensity profile. All combinations of $\text{DC}_{\text{mean}} = \frac{a+b}{2\Lambda_{\text{SWG}}}$ and $\Delta\text{DC} = \frac{a-b}{\Lambda_{\text{SWG}}}$ are simulated and the emission angles θ_z and coupling strengths κ are recorded in b) and c), respectively. A lookup-based inverse design method is employed by analytically calculating the required coupling strengths $\kappa(y)$ (blue line in d)) and local emission angles $\theta_{\text{loc}}(y)$ (red line in d)) along the grating and replicating them using the design sweeps from b) and c).

spatially varying the unit cell, we realize an arbitrary, position-dependent coupling strength $\kappa(y)$ while independently controlling the local emission angle $\theta_{\text{loc}}(y)$. Combining the analytic $\kappa(y)$ -profile synthesis established for conventional grating couplers [11, 32, 33, 34] with the sub-wavelength approach of [31] allows us to reach the very low coupling strengths needed for large beams and, for the first time, to shape them into high-quality collimated Gaussian beams.

In our proposed design scheme, we aim to precisely replicate the local coupling strength $\kappa(y)$ required to emit a Gaussian beam. As has been shown in previous publications [11, 32, 33, 34], the local coupling strength required for a target emission profile $S(y)$ is given by

$$\kappa(y) = \frac{S(y)}{P(-\infty) - \int_{-\infty}^y S(t)dt} \quad (1)$$

where $P(-\infty)$ represents the initial power injected from the waveguide into the grating, with the boundary condition that all power is to be emitted into the beam:

$$\int_{-\infty}^{+\infty} S(y)dy \stackrel{!}{=} P(-\infty). \quad (2)$$

2D simulations using the Lumerical FDTD: 3D Electromagnetic Simulator [35] were performed for various combinations of ridge widths a and b by sweeping the average duty cycle $\text{DC}_{\text{mean}} = (a+b)/2\Lambda_{\text{SWG}}$ and the absolute difference $\Delta\text{DC} = (a-b)/\Lambda_{\text{SWG}}$ over the specified regions in Figures 2b and 2c. Each point in these graphs corresponds to a homogeneous grating consisting of a repeating unit cell. For each single simulation the complex electrical near field $E(y)$ was recorded above the grating. The near field intensities $|E(y)|^2$ were then fitted with an exponential function $\propto \exp(-\kappa y)$ (see Figure 2a), from which the coupling strengths κ were obtained for all designs. By projecting the complex near field $E(y)$ into the far field, the emission angle relative to the z -axis θ_z (see Figure 1b for reference) was obtained by finding the far field peak. The sweep results for the emission angles and coupling strengths of a sweep with a fixed periodicity of $\Lambda = 880$ nm are displayed in Figures 2b and 2c, respectively.

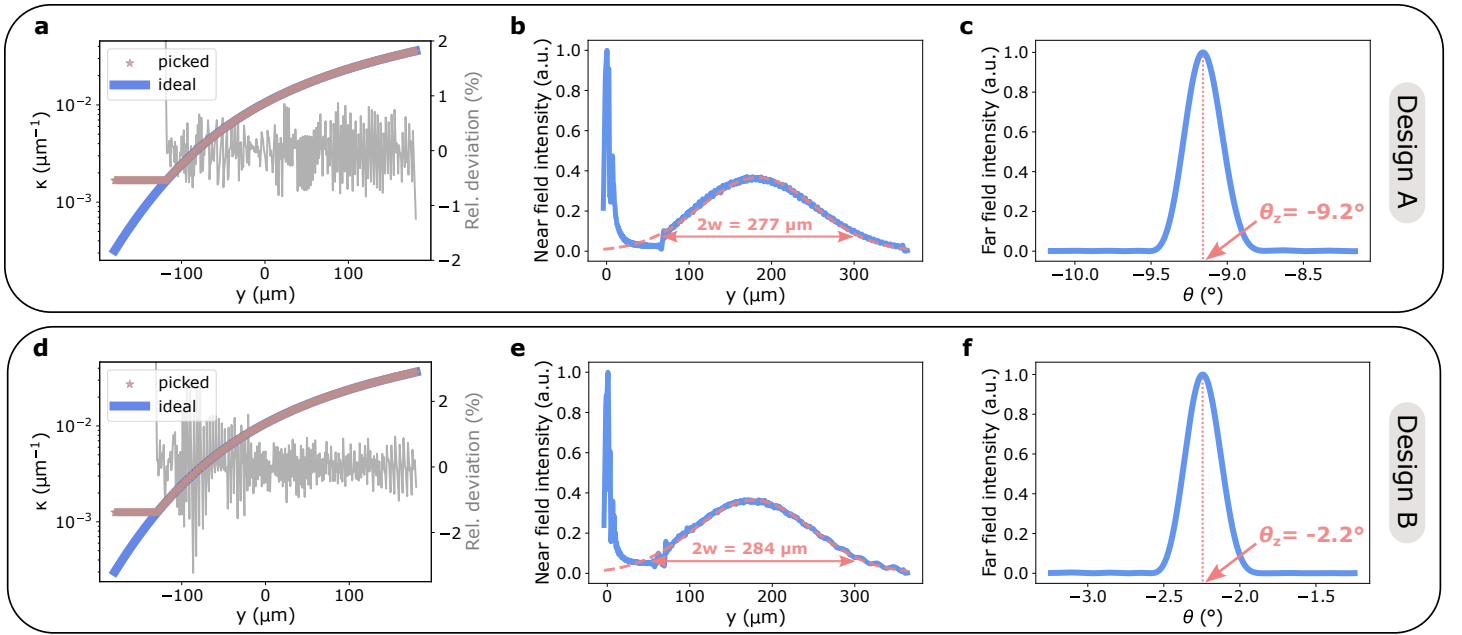


Figure 3: Simulation data of both designs A and B with goal emission angles of $\theta_z^A = -9^\circ$ and $\theta_z^B = -2^\circ$, respectively and a goal beam waist diameter of $2w_0 = 300 \mu\text{m}$. a) and d) custom-picked coupling strengths (orange stars) along the grating and the corresponding ideal values (blue line). b) and e) simulated near field intensity distributions predicting beam waist diameters of $2w_{0,A} = 277 \mu\text{m}$ and $2w_{0,B} = 284 \mu\text{m}$. c) and f) corresponding far field projections, predicting emission angles of $\theta_{z,\text{sim}}^A = -9.2^\circ$ and $\theta_{z,\text{sim}}^B = -2.2^\circ$. The simulated radiation efficiencies are $T_{\text{sim}}^A = T_{\text{sim}}^B = 70\%$.

The desired Gaussian beam's electric field at the grating's plane can be analytically described by $E(y, z = 0) = |E(y, z = 0)| \cdot \exp(-i \cdot \phi(y))$, which for a beam waist of w_0 located at $z = 0$ and a propagation angle of θ_z with respect to the z-axis (see Figure 1b for reference) yields an intensity of

$$S(y) \propto |E(y, z = 0)|^2 = \left| E_0 \frac{1}{\sqrt{1 + \left(\frac{\lambda y \sin(\theta_z)}{\pi w_0^2}\right)^2}} \cdot \exp\left\{-\frac{(y \cos(\theta_z))^2}{w_0^2 \cdot \left(1 + \left(\frac{\lambda y \sin(\theta_z)}{\pi w_0^2}\right)^2\right)}\right\} \right|^2 \quad (3)$$

and

$$\phi(y) = -\left[\frac{2\pi}{\lambda} y \sin(\theta_z) + \frac{2\pi}{\lambda} \frac{(y \cos(\theta_z))^2}{2y \sin(\theta_z) \cdot \left(1 + \left(\frac{\pi w_0^2}{\lambda y \sin(\theta_z)}\right)^2\right)} - \arctan\left(\frac{\lambda y \sin(\theta_z)}{\pi w_0^2}\right) \right], \quad (4)$$

where λ is the wavelength in the medium. If a focusing beam is desired, the equations above can be easily adjusted to account for the location of the waist to be at $z > 0$. $|E(y, z = 0)|^2$ from Equation 3 is then substituted for $S(y)$ in Equation 1 to calculate the resulting coupling strength $\kappa(y)$. Additionally, the phase expression $\phi(y)$ from Equation 4 determines the local y-component $k_y(y)$ of the beam's wave number $k_0 = \frac{2\pi}{\lambda}$, from which in turn the required local emission angle $\theta_{\text{loc}}(y)$ can be calculated:

$$k_y(y) = \frac{d\phi(y)}{dy} \Rightarrow \theta_{\text{loc}}(y) = \arcsin\left(\frac{k_y(y)}{k_0}\right) \quad (5)$$

In this contribution, two designs A and B are evaluated. Both are designed to have a goal beam waist diameter of $2w_0 = 300 \mu\text{m}$. We choose goal emission angles of $\theta_z^A = -9^\circ$ and $\theta_z^B = -2^\circ$ to avoid the strong Bragg reflection associated with vertical coupling and to demonstrate the feasibility of creating custom emission angles. The periods for design A and B were chosen to be $\Lambda_A = 880 \text{ nm}$ and $\Lambda_B = 900 \text{ nm}$, respectively. Representative for both designs, the entire design process for design A is shown in Figures 2b-d. The resulting constant local emission angle of -9° in Figure 2d allows to filter out all homogeneous designs, i.e. combinations of ridge widths a and b , that exhibit an emission angle of $-9 \pm 0.1^\circ$

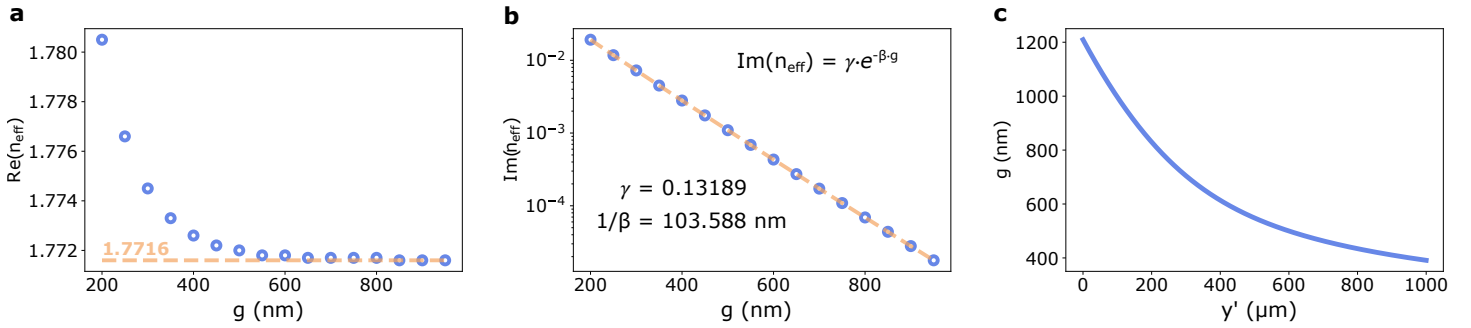


Figure 4: Real (a) and imaginary (b) parts of the TM₀₀ effective mode index as a function of the gap in between the waveguide and the slab region obtained through COMSOL Multiphysics® FEM simulations [36]. c) The analytically derived gap distance as a function of the propagation distance y' along the waveguide.

in the coupling-strength map in Figure 2c. Subsequently, individual unit cells are placed along the y -direction to best fit the required $\kappa(y)$ -function, as indicated by the gray lines in between Figures 2c and 2d.

Figures 3a and 3d show the analytically calculated coupling strength values $\kappa(y)$ (blue line) and the custom picked coupling strengths (orange stars) from the simulation sweeps (Figure 2c) for designs A and B, respectively. For small κ -values below $2 \cdot 10^{-3} \mu\text{m}^{-1}$, the design spaces lacked sufficiently small κ -values, leading to a mismatch at the beginning of the gratings in both cases. However, for the remainder of the gratings, the coupling strengths could be neatly matched with small deviations. This directly translates to the simulated near field intensity profiles in Figures 3b and 3e, which only deviate from a Gaussian shape at the beginning where the required coupling strengths did not match. The near field intensity peak at $y = 0 \mu\text{m}$ is attributed to the jump in refractive index occurring at the slab-grating interface and causes a parasitic, non-directional upwards emission of 13 % and 10 % for designs A and B, respectively, as shown in the supplementary materials. This can be mitigated by employing a gradual transition region, as shown in [31]. The simulated far field emission angles (Figures 3c and 3f) of both designs were determined to be $\theta_{z,\text{sim}}^{\text{A}} = -9.2^\circ$ and $\theta_{z,\text{sim}}^{\text{B}} = -2.2^\circ$, closely matching the goal angles of $\theta_z^{\text{A}} = -9^\circ$ and $\theta_z^{\text{B}} = -2^\circ$, respectively, while showing radiation efficiencies of $T_{\text{sim}}^{\text{A}} = 70\%$ and $T_{\text{sim}}^{\text{B}} = 70\%$. Since the proposed design scheme uses fully etched gratings the emission from the grating is equally split into the positive and negative z -directions. The light emitted downwards experiences some reflection at the high-index-contrast interface of the buried oxide layer and the Si handle layer. Depending on the emission angle and thickness of the buried layer, the reflected light interferes with the light which is emitted directly upwards from the chip, leading to simulated radiation efficiencies upwards of 50 %. This value can still be optimized if the buried oxide layer thickness can be chosen arbitrarily. In our case, this value was fixed to 2 μm due to the fabrication process used.

2.2 Evanescent mode converter

The longitudinal beam shape is controlled by the grating design presented above. To achieve the same beam profile in the transverse direction (along the x -coordinate in Figure 1a), an evanescent mode converter was designed using the design approach from [25]. For the sake of thoroughness, the key steps are explained here. The FEM solver from COMSOL Multiphysics®' Wave Optics Module [36] was used to calculate the waveguide's 2D mode profile as a function of the gap distance g between the waveguide and the slab region. The waveguide itself was assumed to be lossless and the radiation of the mode's energy into the slab due to evanescent tunneling was accounted for by introducing optical losses in the slab. For each gap distance, the real and imaginary parts of the mode's effective index were recorded and are displayed in Figures 4a and 4b, respectively. The real part of the mode index will determine the emission angle θ_{slab} into slab according to

$$\cos(\theta_{\text{slab}}) = \Re\{n_{\text{eff}}^{\text{wg}}\} / \Re\{n_{\text{eff}}^{\text{slab}}\} \quad (6)$$

and the imaginary part determines the power loss factor of the mode $\alpha(y') = \frac{4\pi}{\lambda_0} \Im\{n_{\text{eff}}^{\text{wg}}\}$ [25].

The resulting gap function for a Gaussian slab mode $S(y') \sim \exp(-2\frac{(y'-y'_0)^2}{\tilde{w}^2})$ with waist \tilde{w} and center position y'_0 is then given by:

$$g(y') = -\frac{1}{\beta} \ln \left(\frac{\lambda_0}{\sqrt{2}\gamma\tilde{w}\pi^{3/2}} \frac{e^{-2\frac{(y'-y'_0)^2}{\tilde{w}^2}}}{1 - \operatorname{erf}\left\{\sqrt{2}\frac{y'-y'_0}{\tilde{w}}\right\}} \right) \quad (7)$$

with β, γ being the fit coefficients from Figure 4b. For an effective slab beam waist diameter of $2w_{\text{slab}} = 300 \mu\text{m}$, the slab emission angle needs to be taken into account by setting the waist in the equation above to $\tilde{w} = w_{\text{slab}}/\sin(\theta_{\text{slab}})$. The real part of the mode index and therefore the slab emission angle was assumed to be constant, i.e. Equation 6 then yields $\theta_{\text{slab}} = \cos^{-1}(1.7716/2.0537) \approx 30.36^\circ$, which is a good approximation due to the resulting gap profile exhibiting values larger than 400 nm (Figure 4c).

3 Experimental Results

To experimentally validate the design process described above, the two different grating designs A and B with design emission angles of $\theta_z^A = -9^\circ$ and $\theta_z^B = -2^\circ$ and design waist diameters of $2w_0 = 300 \mu\text{m}$ were fabricated using the Applied Nanotools Inc. NanoSOI Fabrication Service [37], as described in the Methods section. The evanescent mode converter was identical for both designs and exhibited the gap function from Figure 4c.

The beam cross sections were imaged from $z = 0 \text{ mm}$ (near field) up to $z = 80 \text{ mm}$ in 1 mm steps. For visual clarity, the beam slices are shown from $z = 30 \text{ mm}$ up to $z = 50 \text{ mm}$ in 2 mm steps in Figures 5a and 5b. By tracking the beam centers, the emission angles were determined to be $\theta_{z,\text{exp}}^A = -9.4^\circ$ and $\theta_{z,\text{exp}}^B = -2.7^\circ$, closely matching the simulated emission angles $\theta_{z,\text{sim}}^A = -9.2^\circ$ and $\theta_{z,\text{sim}}^B = -2.2^\circ$. The radiation efficiencies were determined to be $T_{\text{exp}}^A = 31 \%$ and $T_{\text{exp}}^B = 49 \%$ (see Methods section for details), below the simulated value of $T_{\text{sim}} = 70 \%$. Part of this reduction is attributed to the parasitic emission at the slab-grating interface. As shown in the supplementary materials, this non-directional emission is simulated to amount to 13% and 10% for designs A and B, respectively, and can be mitigated by a gradual transition region like the one shown in [31]. For fully-etched gratings, the emission is in principle split equally into the $+z$ and $-z$ directions, which would limit the upward radiation efficiency to 50%. The reflection at the BOX-substrate interface can lift this limit: depending on the emission angle and the oxide thickness, the downward-emitted light interferes constructively with the upward emission and allows efficiencies above 50%. The remaining gap between the measured efficiencies and this expectation is, however, dominated by the way the radiation efficiency is extracted rather than by the coupler itself. As detailed in the Methods section, the efficiency is obtained by taking into account the estimated fiber-array-to-chip coupling efficiency, which relies on vendor-specified parameters. (For design A, only TE-polarization measurement data was available. For TM-polarization, the vendor estimated an additional loss of 0.5 dB) Further, designs A and B were located on separate chips with different edge-coupling schemes, so their absolute efficiency values are not directly comparable, and the value for design B represents a lower bound. We therefore treat these figures as order-of-magnitude estimates carrying a substantial systematic uncertainty. Notably, the central result of this work, the beam quality, is measured directly from the free-space beam and is independent of these in-coupling estimates.

Figures 5c and 5d show the respective near field images of the beams with line profiles corresponding to the field distributions caused by the grating design (red profiles, along y) and the evanescent mode converter (gray profiles, along x). In both cases, Gaussian-like intensity distributions are observed for the red y -profiles, with waist diameters of $314 \mu\text{m}$ and $370 \mu\text{m}$, respectively. While design A matches the target waist of $300 \mu\text{m}$ to within 5%, the larger deviation of design B is most likely related to its shallower emission angle of -2° , which lies closer to the vertical Bragg condition. In this regime the local coupling strength is more sensitive to fabrication-induced deviations, and the initial region of insufficient κ -matching (Section 2.1) has a stronger effect on the resulting beam width, broadening the effective waist along the grating direction. The distinct emission peak at the beginning of the grating in the

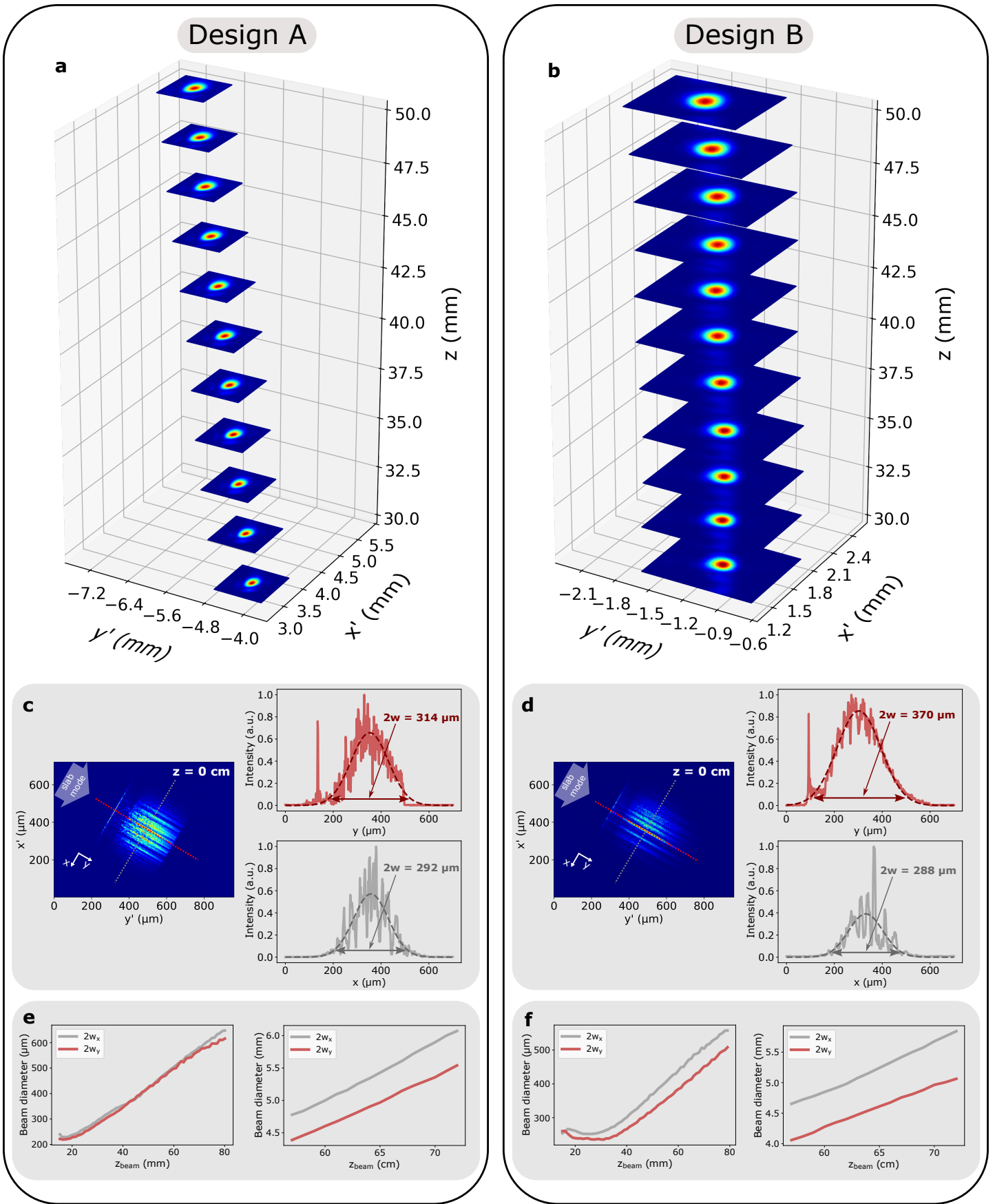


Figure 5: Experimental beam analysis for both designs. a) and b) show the imaged beam intensity slices from 30 mm to 50 mm above the chips. c) and d) show the analysis of the near field intensity along (gray lines) and perpendicular (red lines) to the grating ridges. e) and f) show the beam waist diameters along x and y acquired from Gaussian fits of the line profiles with maximum 2σ -uncertainties of $\pm 8.28 \mu\text{m}$ and $\pm 76.6 \mu\text{m}$ for the plots with $15 \text{ mm} < z_{\text{beam}} < 80 \text{ mm}$ and $57 \text{ cm} < z_{\text{beam}} < 72 \text{ cm}$, respectively.

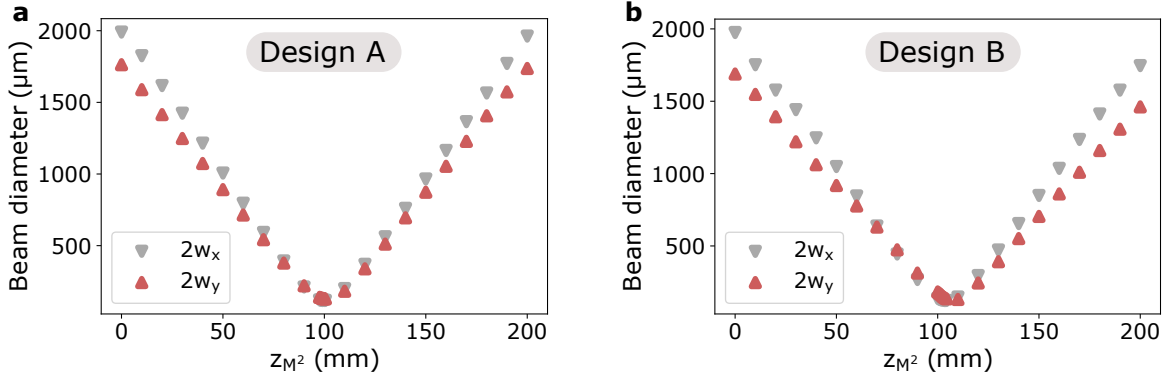


Figure 6: ISO 11146 [38] compliant M^2 measurements for a) design A and b) design B. The beams emitted from the chip were collimated using a plano-convex lens with a focal length of $f_c = 500$ mm placed at a distance of ≈ 50 cm from the chip and were then focused inside of the M^2 measurement system with a second plano-convex lens with $f_{M^2} = 250$ mm. A spherical aperture with a diameter of 8 mm was used to filter out side lobes which appeared along the x -directions. Measurements along the x - and y -axes correspond to the evanescent mode converter and the grating, respectively. The spatial coordinate z_{M^2} refers to the position of the linear stage within the system. The ISO-compliant hyperbolic fits yield values of $M_{x,A}^2 = 1.04$, $M_{y,A}^2 = 1.10$, $M_{x,B}^2 = 1.05$, $M_{y,B}^2 = 1.09$ with an uncertainty of $\pm 5\%$.

red profiles can be attributed to the jump in the effective mode index that occurs at the slab-grating interface and causes parasitic emission of the order of 10% (see supplementary information). The transverse x -profiles, set by the evanescent mode converter, are unaffected by this and exhibit Gaussian-like distributions with waist diameters of 292 μm and 288 μm , respectively, closely matching the goal waist of 300 μm for both designs. Additionally, an interference pattern along the x -profiles can be observed. This we attribute to the slab mode not being perfectly vertically incident to the grating coupler. This is likely caused by the evanescent mode converter design: a deviation of the simulated waveguide and slab mode indices from the real ones causes a change in the propagation angle of the slab mode according to Equation 6. This causes a non-zero x -component of the slab wave vector along the grating ridges, which oscillates as a standing wave along the x -direction. Since the aim is to demonstrate collimated Gaussian beams, the analysis of the far field emissions of both gratings are of interest. Figures 5e and 5f show the evolution of the beam waist diameters of the beams along both the x - and y -axes as a function of the beam propagation distance z_{beam} . For each image, the center position of the beam and the beam waists along the two grating axes x and y were determined by fitting a Gaussian $\propto \exp(-2(n - n_0)^2/w_n^2)$, $n = x, y$ to the corresponding line profiles. Due to the non-vertical emission angle, the z -coordinate was adjusted to point along the propagation direction, $z_{\text{beam}} = z/\cos(\theta_{z,\text{exp}})$, and the waist diameter along the x -axis was corrected accordingly, $2w_x = 2w_{x,\text{fit}} \cdot \cos(\theta_{z,\text{exp}})$. The graphs in Figures 5e and 5f show the analysis for $15 \text{ mm} < z < 80 \text{ mm}$ and $57 \text{ cm} < z_{\text{beam}} < 72 \text{ cm}$. Since the images up to a height of approximately 15 mm showed near field interference patterns, which prohibited proper Gaussian fits and beam center calculations, the analysis starts at a height of $z_{\text{beam}} = 15 \text{ mm}$. The analysis of the beams up to a height of 80 mm was conducted using the microscope setup with a 10X objective, whereas for the analysis in the range of 57 cm to 72 cm the SWIR camera was directly placed in the beam path without any magnifying optics.

In order to quantify the quality of the beams generated by the two grating designs, ISO 11146 [38] compliant M^2 measurements were conducted. The beam quality factor M^2 is defined by

$$M^2 = \frac{2w_m \Theta_m}{2w_0 \Theta_0} \Big|_{w_m = w_0} \frac{\Theta_m}{\Theta_0} \quad (8)$$

where w_m and Θ_m represent the measured beam waist and divergence angle and Θ_0 the beam waist and divergence angle of an ideal Gaussian beam. M^2 thus quantitatively describes how close the beam profile is to an ideal Gaussian. The measurements were conducted using a commercial M^2 Measurement System (see Methods section) which employed a scanning slit beam profiler. The beam profiler's measurement axes were aligned to the axes corresponding to the grating design's emission profile (y -axis in Fig-

Table 1: This table compares the simulation and experimental results of both designs regarding their emission angles θ_z , near field waist diameters $2w_0$, radiation efficiency T and beam quality factors M^2 ($\pm 5\%$) along the x- and y-axes.

		θ_z (°)	$2w_0$ (μm)	T (%)	M_x^2	M_y^2
Design A	Goal	-9	300	> 50	1.0	1.0
	Simulation	-9.2	277	70	-	-
	Experiment	-9.4	314	31	1.04	1.10
Design B	Goal	-2	300	> 50	1.0	1.0
	Simulation	-2.2	284	70	-	-
	Experiment	-2.7	370	≥ 49	1.05	1.09

ure 1a) and the evanescent mode converter’s emission profile (x-axis in Figure 1a), respectively. Along the x-direction, when focusing the beam during the M^2 -measurement, the beams’ side lobes significantly interfere with the main profile around the focal position, prohibiting proper M^2 measurement of the x-axes. Therefore, a spherical aperture with a diameter of 8 mm was placed in the beam path (see Figure 7c) to suppress these side lobes. The resulting beam quality factors in the x-direction (corresponding to the evanescent mode converter) and y-direction (corresponding to the grating design) of designs A and B were determined to be $M_{x,A}^2 = 1.04$, $M_{y,A}^2 = 1.10$, $M_{x,B}^2 = 1.05$, $M_{y,B}^2 = 1.09$ with an uncertainty of $\pm 5\%$, thus showing excellent beam properties. Table 1 shows a comparison of the goal, simulated and experimental values of both designs, which overall yield excellent agreement.

4 Methods

Chip fabrication

The chips were fabricated on SOI multi-project wafers by Applied Nanotools (ANT) [37] and consisted of a Si-handle-layer, a SiO_2 buried oxide layer and a Si device layer with thicknesses of 725 μm , 2 μm and 220 nm, respectively. The device layer was patterned (full device layer etch) using 100 keV electron beam lithography and an SiO_2 top oxide cladding with a thickness of 2.2 μm was deposited on top of the patterned device layer using a plasma-enhanced chemical vapor deposition process. A scanning-electron microscope image of the grating ridges and an optical microscope image of a grating coupler are shown in Figures 7a and 7b, respectively.

Beam characterization

The experimental setup used to characterize the beam profiles is shown in Figure 7c. The custom microscope setup is built around the Thorlabs Cerna microscope platform and uses three different beam paths for visible microscopy (VIS CMOS camera: Thorlabs CS165MU/M), SWIR microscopic beam imaging (SWIR InGaAs camera: NIT WiDy SenS 640) and measuring the M^2 beam quality factor. The microscope is equipped with long working distance objectives (Mitutoyo M Plan Apo NIR 5X (NA = 0.14) and Mitutoyo M Plan Apo NIR 10X (NA = 0.26)) with a transmission window of 480 nm to 1800 nm and are used together with 200 mm focal length tube lenses (Thorlabs WFA4100 for VIS and Thorlabs TTL200-S8 for SWIR). In this work only the 10X objective was used since the emission angle of Design A (-9.4°) lay outside of the acceptance cone of the 5X objective, given by $\Theta_{\text{max},5\text{X}} = \arcsin(\text{NA}) \approx 8.05^\circ$. The chips were mounted on a vacuum chip mount fixed to an optical table. The microscope was placed on a long-travel z-stage (Standa MT195), which was mounted on an xy-stage (Standa 8MTF-200) with step resolutions of 12.5 μm and 2.5 μm , respectively. The microscope setup was used to image the beam in the first 80 mm above the chip. To measure the beam quality factors M^2 and beam propagation at larger distances, an additional retractable mirror was placed above the chip to guide the beam parallel to the optical table. For the M^2 measurements, the beam was collimated using a plano-convex collimation lens with $f_c = 500$ mm and the x-axis side lobes of the beam were cropped using a spherical 8 mm aperture. The M^2 measurements were conducted using the commercial Thorlabs M2 Measure-

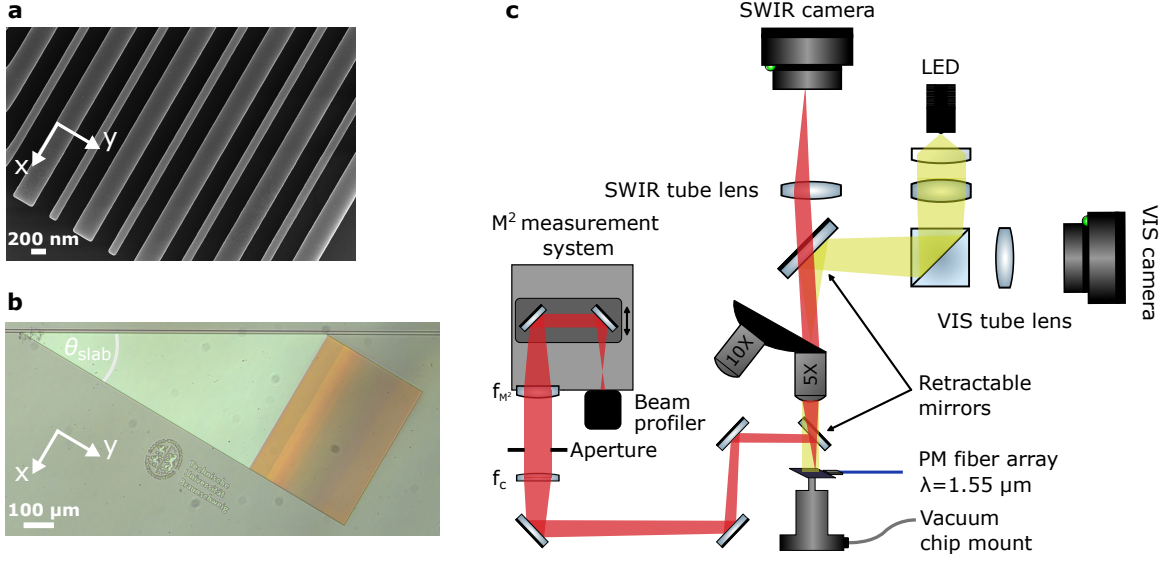


Figure 7: a) Scanning electron microscopic image of the grating ridges at the end of a grating acquired by ANT [37] after etching and b) an optical microscopic image of the mode converter and grating of design A. c) The optical setup used to characterize the designs. Three operational modes can be chosen by inserting/retracting mirrors: (i) optical microscopic imaging, (ii) SWIR microscopic beam imaging and (iii) measuring M^2 beam quality.

ment System M2MS-BP209IR, which consists of two mirrors mounted on a linear stage and a scanning slit beam profiler. The focusing plano-convex lens shipped with the system had a focal length of $f_{M^2} = 250$ mm and is supposed to allow the beam profiler to image the beam around its focus by moving the linear stage. However, the divergences of the beams under test were too large, causing the focus to be out of the range of the system. Thus, an additional collimating lens with $f_c = 500$ mm was placed at a distance of 500 mm from the chip to decrease the divergence of the beam, which placed the focus in the center of the stage’s range (see Figure 6 for reference). The x- and y-axes of the beam profiler were aligned with the x- and y-axes of the beam (see Figure 5 for reference). Subsequently, the linear stage scanned its entire range and allowed the beam profiler to track the intensity profiles along the two axes and calculate the waist diameters along x and y at every position. All M^2 measurements were ISO 11146 compliant. For measuring the beam propagation in the far field, the M^2 setup including the collimation lens was removed and the SWIR camera was placed in the beam path at distances of 57 cm to 72 cm from the chip.

Designs A and B were located on two different chips and used different edge coupling methods: For design A, the chip was equipped with facet-attached micro lenses (FaMLs) from DreamPhotonics [39] which facilitate the alignment of the chip and fiber-array. Consequently, a lensed, polarization maintaining fiber array from DreamPhotonics was used for in-coupling. For the case of an SOI-chip fabricated by Applied Nanotools with the additional FaMLs, DreamPhotonics reports an average insertion efficiency of $T = 64.2\%$ for TE polarization. For TM polarization DreamPhotonics estimates an additional polarization-dependent loss of 11%, resulting in a total coupling efficiency of $T = 64.2\% \cdot 89\% = 57.1\%$. Additionally, a power splitter with an experimentally determined splitting ratio of 18.7%/81.3% was placed before the waveguide reaches the evanescent mode converter. Thus the total transmission from fiber array to the grating (assuming $T = 100\%$ for the mode converter) is $T = 57.1\% \cdot 18.7\% = 10.7\%$. The power emitted from the fiber array and the emitted power 7 cm above the chip were measured to be 2.541 mW and 83.0 μ W, respectively. Thus, the estimated radiation efficiency of design A is $T_A = 83.0 \mu\text{W} / 2,541 \mu\text{W} / 0.107 \approx 31\%$. For design B, nano-tapered edge couplers from the ANT PDK were used with a lensed, focusing PM fiber array from PHIX with a focal mode field diameter (MFD) of 3.6 μ m. ANT reports an average insertion efficiency of $T = 51.3\%$ when using a lensed PM fiber with a MFD of 2.5 μ m. Thus, the calculated radiation efficiency for design B represents a lower boundary for the actual efficiency. The power emitted from the fiber array and the power 7 cm above the grating were measured

to be 2.963 mW and 0.744 mW, respectively. The resulting lower boundary for the radiation efficiency is therefore $T_B \geq 0.744 \text{ mW} / 2.963 \text{ mW} / 0.513 \approx 49 \%$.

5 Conclusion

We have demonstrated silicon-on-insulator grating couplers that emit collimated Gaussian beams with diameters of several hundred micrometers at $\lambda = 1.55 \mu\text{m}$. These couplers are designed by tailoring the local coupling strength of a sub-wavelength grating along its length and independently controlling the local emission angle. Beam quality measurements, conducted in accordance with ISO 11146 [38], yield $M^2 \leq 1.10 (\pm 5 \%)$. Although large-area grating couplers have previously been reported, their beam quality has, to our knowledge, not been quantified. The present work establishes near-ideal beam quality as an achievable and verifiable property of this coupler class.

The framework can be directly adapted to other target field distributions, such as flat-top beams or higher-order modes, by substituting the desired complex electric field in Equation 3. This adaptability makes meta-grating couplers a practical chip-to-free-space interface for applications sensitive to mode matching, including coupling into high-finesse resonators and forming optical traps. A logical next step is to compensate for residual emission-angle variation using metasurface-based wavefront correction, which would further enhance the achievable mode overlap.

Supporting Information

Supporting Information is available from the author.

Acknowledgements

This project has received funding from the European Research Council (ERC) under the European Union's Horizon Europe research and innovation program (Project Number [101170022]). This work is partially funded by the Deutsche Forschungsgemeinschaft (DFG, German Research Foundation) under Germany's Excellence Strategy – EXC-2123 Quantum-Frontiers – 390837967. M.S. acknowledges support from the Max Planck School of Photonics.

Supplementary Information

Figures 8 and 9 show the origin of the near field emission peak observed in both the simulations and experimental measurements of the meta-grating designs. Due to the abrupt refractive index change at the beginning of the grating non-directional emission can be observed. The amount of power that gets radiated depends on the difference in refractive index (Figure 9). For the designs discussed in this contribution, the refractive index of the slab waveguide is that of silicon, i.e. $n_1 = 3.476$. The effective refractive index of the meta-grating can be estimated since the average duty cycle of each cell DC_{mean} remains approximately constant along the grating. The effective refractive index for TM-polarized light can then be estimated by [40]:

$$n_{\text{eff}} \approx \frac{n_1 \cdot n_2}{\sqrt{DC \cdot n_2^2 + (1 - DC) \cdot n_1^2}} \quad (9)$$

For designs A and B, the average duty cycles of $DC_{\text{mean}}^A = 0.5$ and $DC_{\text{mean}}^B = 0.625$ yield effective indices of $n_{\text{eff}}^A = 1.886$ and $n_{\text{eff}}^B = 2.079$, corresponding to refractive index jumps of $\Delta n^A = 3.476 - 1.886 = 1.590$ and $\Delta n^B = 3.476 - 2.079 = 1.397$. According to Figure 9, these jumps cause parasitic emissions of 13% and 10% for designs A and B, respectively.

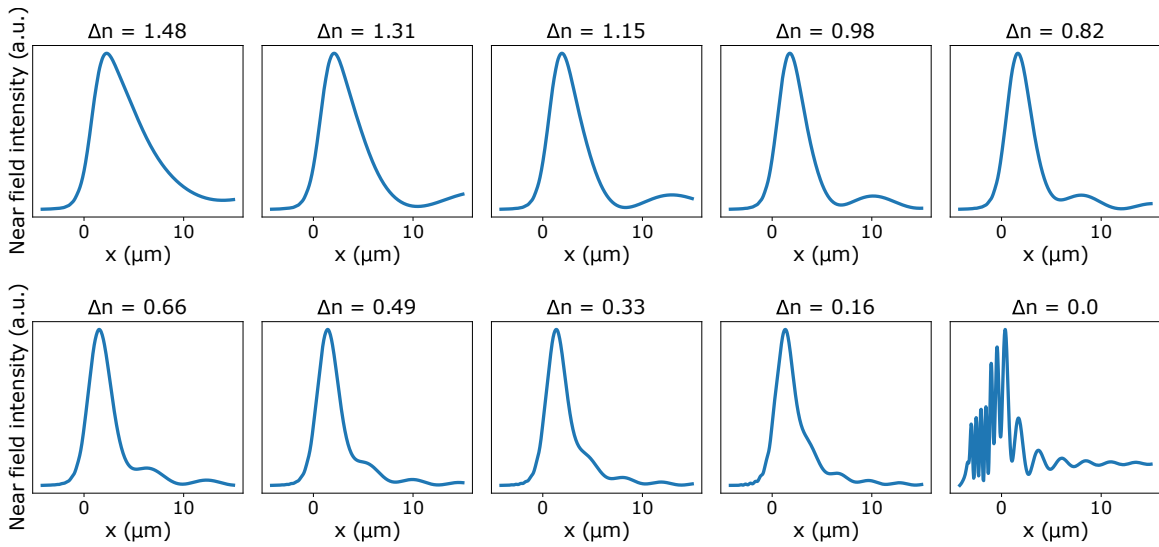


Figure 8: 2D-FDTD-simulations of normalized near field intensities above a waveguide as a function of $\Delta n = n_1 - n_2$, which abruptly changes its refractive index from silicon ($n_1 = 3.476$) to a lower index of n_2 at $x = 0$. The waveguide's height is 220 nm and the top and bottom oxide layers consist of SiO_2 with a refractive index of 1.444 at a wavelength of $\lambda = 1.55 \mu\text{m}$. These simulations show the origin of the emission peak of the grating designs shown in this contribution. The polarization was set to TM.

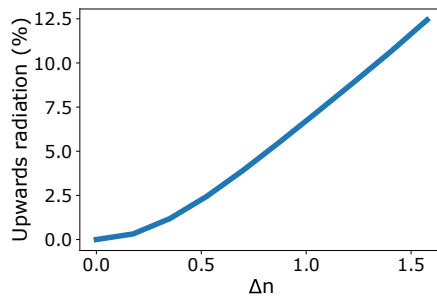


Figure 9: The upwards (+z) emitted radiation resulting from the abrupt waveguide transitions from Figure 8 as a function of Δn .

References

- [1] Xia Chen, Milan M. Milosevic, Stevan Stanković, Scott Reynolds, Thalía Domínguez Bucio, Ke Li, David J. Thomson, Frederic Gardes, and Graham T. Reed. The emergence of silicon photonics as a flexible technology platform. *Proceedings of the IEEE*, 106:2101–2116, 2018.
- [2] Shawn Yohanes Siew, Bo Li, Feng Gao, Hai Yang Zheng, Wenle Zhang, Pengfei Guo, Shawn Wu Xie, Apu Song, Bin Dong, Lian Wee Luo, Chao Li, Xianshu Luo, and Patrick Guo-Qiang Lo. Review of silicon photonics technology and platform development. *Journal of Lightwave Technology*, 39:4374–4389, 2021.
- [3] Sudip Shekhar, Wim Bogaerts, Lukas Chrostowski, John E. Bowers, Michael Hochberg, Richard Soref, and Bhavin J. Shastri. Roadmapping the next generation of silicon photonics. *Nature Communications*, 15(1):751, 2024.
- [4] David Thomson, Aaron Zilkie, John E Bowers, Tin Komljenovic, Graham T Reed, Laurent Vivien, Delphine Marris-Morini, Eric Cassan, Leopold Viot, Jean-Marc Fédéli, Jean-Michel Hartmann, Jens Schmid, Dan-Xia Xu, Frederic Boeuf, Peter O’Brien, Goran Mashanovich, and Miloš Nedeljković. Roadmap on silicon photonics. *Journal of Optics*, 18(7):073003, 2016.
- [5] Katrien De Vos, Irene Bartolozzi, Etienne Schacht, Peter Bienstman, and Roel Baets. Silicon-on-insulator microring resonator for sensitive and label-free biosensing. *Optics Express*, 15(12):7610–7615, 2007.
- [6] Johannes Milvich, Daria Kohler, Wolfgang Freude, and Christian Koos. Integrated phase-sensitive photonic sensors: a system design tutorial. *Advances in Optics and Photonics*, 13(3):584–642, 2021.
- [7] Xiaosheng Zhang, Kyungmok Kwon, Johannes Henriksson, Jianheng Luo, and Ming C. Wu. A large-scale microelectromechanical-systems-based silicon photonics lidar. *Nature*, 603:253–258, 2022.
- [8] Yue Wang, Yu Wang, Zeyang Zhang, Chunhui Wang, Jinyong Wang, Kuang Zhang, Xing Yang, Guohui Yang, and Yu Zhang. Design of free-space dual-polarization receiving antenna with deep learning for coherent photonic-integrated lidar. *ACS Photonics*, 12:5658–5667, 2025.
- [9] Jianwei Wang, Fabio Sciarrino, Anthony Laing, and Mark G. Thompson. Integrated photonic quantum technologies. *Nature Photonics*, 14(5):273–284, 2020.
- [10] Theodor Tamir and Song Tsuen Peng. Analysis and design of grating couplers. *Applied physics*, 14(3):235–254, 1977.
- [11] Dirk Taillaert, Peter Bienstman, and Roel Baets. Compact efficient broadband grating coupler for silicon-on-insulator waveguides. *Optics Letters*, 29:2749–2751, 2004.
- [12] Frederik Van Laere, Gnther Roelkens, Melanie Ayre, Jonathan Schrauwen, Dirk Taillaert, Dries Van Thourhout, Thomas F. Krauss, and Roel Baets. Compact and highly efficient grating couplers between optical fiber and nanophotonic waveguides. *Journal of Lightwave Technology*, 25(1):151–156, 2007.
- [13] Logan Su, Rahul Trivedi, Neil V. Saprà, Alexander Y. Piggott, Dries Verdecruysse, and Jelena Vučković. Fully-automated optimization of grating couplers. *Optics Express*, 26(4):4023–4034, 2018.
- [14] Lirong Cheng, Simei Mao, Zhi Li, Yaqi Han, and H. Y. Fu. Grating couplers on silicon photonics: Design principles, emerging trends and practical issues. *Micromachines*, 11, 2020.
- [15] Lvyi Zhong, Maoqing Guo, Shilong Li, Yuhang Chen, Jie Li, Jitao Li, and Dingyu Yang. Progress of grating couplers for light exchange between space and on-chip. *Advanced Optical Materials*, 13(30):e01171, 2025.

- [16] Zheng Luo, Travis C. Briles, Zachary L. Newman, Aidan R. Jones, Andrew R. Ferdinand, Sindhu Jammi, Grisha Spektor, David R. Carlson, Akash Rakholia, Dan Sheredy, Parth Patel, Martin M. Boyd, Chad Ropp, Daron Westly, Vladimir A. Aksyuk, Wenqi Zhu, Junyeob Song, Amit Agrawal, and Scott B. Papp. A scalable infrastructure for strontium optical clocks with integrated photonics, 2026. arXiv: <https://arxiv.org/abs/2604.03229>.
- [17] Andrei Isichenko, Nitesh Chauhan, Debapam Bose, Jiawei Wang, Paul D. Kunz, and Daniel J. Blumenthal. Photonic integrated beam delivery for a rubidium 3d magneto-optical trap. *Nature Communications*, 14(1):3080, 2023.
- [18] Chad Ropp, Wenqi Zhu, Alexander Yulaev, Daron Westly, Gregory Simelgor, Akash Rakholia, William Lunden, Dan Sheredy, Martin M. Boyd, Scott Papp, Amit Agrawal, and Vladimir Aksyuk. Integrating planar photonics for multi-beam generation and atomic clock packaging on chip. *Light: Science & Applications*, 12(1):83, 2023.
- [19] Alexander Yulaev, Chad Ropp, John Kitching, Vladimir A. Aksyuk, and Matthew T. Hummon. Chip-scale sub-doppler atomic spectroscopy enabled by a metasurface integrated photonic emitter. *Applied Physics Letters*, 125(12):121114, 2024.
- [20] Matthew T. Hummon, Songbai Kang, Douglas G. Bopp, Qing Li, Daron A. Westly, Sangsik Kim, Connor Fredrick, Scott A. Diddams, Kartik Srinivasan, Vladimir Aksyuk, and John E. Kitching. Photonic chip for laser stabilization to an atomic vapor with 10^{-11} instability. *Optica*, 5:443, 2018.
- [21] Dana Z. Anderson. Alignment of resonant optical cavities. *Applied Optics*, 23(17):2944–2949, 1984.
- [22] Daniel J. Blumenthal, Andrei Isichenko, and Nitesh Chauhan. Enabling photonic integrated 3d magneto-optical traps for quantum sciences and applications. *Optica Quantum*, 2(6):444–457, 2024.
- [23] Marcel N. Kosch, Luca Asteria, Henrik P. Zahn, Klaus Sengstock, and Christof Weitenberg. Multi-frequency optical lattice for dynamic lattice-geometry control. *Physical Review Research.*, 4:043083, Nov 2022.
- [24] Renhao Tao, Maximilian Ammenwerth, Flavien Gyger, Immanuel Bloch, and Johannes Zeiher. High-fidelity detection of large-scale atom arrays in an optical lattice. *Physical Review Letters*, 133:013401, Jul 2024.
- [25] Sangsik Kim, Daron A. Westly, Brian J. Roxworthy, Qing Li, Alexander Yulaev, Kartik Srinivasan, and Vladimir A. Aksyuk. Photonic waveguide to free-space gaussian beam extreme mode converter. *Light: Science and Applications*, 7, 2018.
- [26] Chad Ropp, Alexander Yulaev, Daron Westly, Gregory Simelgor, and Vladimir Aksyuk. Metagrating outcouplers for optimized beam shaping in the visible. *Optics Express*, 29:14789, 2021.
- [27] Alexander Yulaev, Sangsik Kim, Qing Li, Daron A. Westly, Brian J. Roxworthy, Kartik Srinivasan, and Vladimir A. Aksyuk. Exceptional points in lossy media lead to deep polynomial wave penetration with spatially uniform power loss. *Nature Nanotechnology*, 17(6):583–589, 2022.
- [28] Yoav Livneh, Ami Yaacobi, and Meir Orenstein. Two-dimensional quasi periodic structures for large-scale light out-coupling with amplitude, phase and polarization control. *Optics Express*, 30:8425, 2022.
- [29] Heqing Huang, Adam C. Overvig, Yuan Xu, Stephanie C. Malek and Cheng Chia Tsai, Andrea Alù, and Nanfang Yu. Leaky-wave metasurfaces for integrated photonics. *Nature Nanotechnology*, pages 580–588, 2023.
- [30] Alexander Yulaev, Daron A. Westly, and Vladimir A. Aksyuk. Surface-normal free-space beam projection via slow-light standing-wave resonance photonic gratings. *ACS Photonics*, 10(4):945–952, 2023.

- [31] Miguel Barona-Ruiz, Laureano Moreno-Pozas, Pablo Ginel-Moreno, Alejandro Ortega-Moñux, José de Oliva-Rubio, Íñigo Molina-Fernández, J. Gonzalo Wangüemert-Pérez, and Robert Halir. Large beam size grating coupler in silicon-on-insulator using fully etched subwavelength gratings. *Laser & Photonics Reviews*, 19:2401775, 2025.
- [32] Attila Mekis, Steffen Gloeckner, Gianlorenzo Masini, Adithyaram Narasimha, Thierry Pinguet, Subal Sahni, and Peter De Dobbelaere. A grating-coupler-enabled cmos photonics platform. *IEEE Journal on Selected Topics in Quantum Electronics*, 17:597–608, 2011.
- [33] Karan K. Mehta and Rajeev J. Ram. Precise and diffraction-limited waveguide-to-free-space focusing gratings. *Scientific Reports*, 7(1):2019, 2017.
- [34] Zhexin Zhao and Shanhui Fan. Design principles of apodized grating couplers. *Journal of Lightwave Technology*, 38(16):4435–4446, 2020.
- [35] Lumerical Inc. FDTD: 3D electromagnetic simulator.
- [36] COMSOL Multiphysics[®] v. 6.4, 2025. COMSOL AB, Stockholm, Sweden.
- [37] Applied Nanotools Inc., Applied Nanotools NanoSOI Fabrication Service. <https://www.appliednt.com/nanosoi-fabrication-service/>. accessed: 06/12/2026.
- [38] ISO. Lasers and laser-related equipment — Test methods for laser beam widths, divergence angles and beam propagation ratios - Part 1: Stigmatic and simple astigmatic beams. International Standard ISO 11146-1:2021, International Organization for Standardization, Geneva, Switzerland, 2021.
- [39] Dream Photonics Inc. <https://dreamphotonics.com/facet-attached-microlenses/>. accessed: 06/12/2026.
- [40] Pavel Cheben, Robert Halir, Jens H. Schmid, Harry A. Atwater, and David R. Smith. Subwavelength integrated photonics. *Nature*, 560(7720):565–572, 2018.